PHYSICAL REVIEW B VOLUME 43, NUMBER 10 1 APRIL 1991

Scanning tunneling microscopy and spectroscopy of Bi-Sr-Ca-Cu-O 2:2:1:2 high-temperature superconductors

C. K. Shih,* R. M. Feenstra, and G. V. Chandrashekhar
IBM Research Division, Thomas J. Watson Research Center, P.O. Box 218, Yorktown Heights, New York 10598

(Received 29 October 1990)

We have used scanning tunneling microscopy and spectroscopy to investigate the surface-topographic and electronic properties of Bi-Sr-Ca-Cu-O 2:2:1:2 compounds. Even though there are two atoms (Bi and O) per lattice point, only one corrugation maximum per lattice point is observed. Polarity-dependent images show that the corrugations of the images taken at opposite polarities are in phase. We discuss possible explanations for this observation of in-phase corrugations at opposite polarities. Spectroscopic data were obtained at both high and low sample biases. Our data show that the density of surface electronic states near the Fermi level is about 3–4 orders of magnitude smaller than that of a typical metal. These states are only detectable when the stabilization voltage of the tunnel junction is low (< 1.5 V). The conductivity near zero bias is extremely nonlinear, consistent with a nonmetallic surface layer. Vacuum resonant tunneling studies show that at these low-bias voltages the tip-to-sample distance is very small ($\sim 3-6$ Å). This small tip-to-sample distance implies that the conductivity we detect near zero bias might result from the underlying CuO layer. We find evidence of bias-field penetration into the sample, implying that the surface density of states near the Fermi level is too small to screen out the electric field.

I. INTRODUCTION

During the past 2 years the application of scanning tunneling microscopy (STM) and spectroscopy to Bi-Sr-Ca-Cu-O 2:2:1:2 high-temperature superconductors has provided valuable data, but has also raised some interesting questions. STM images with atomic resolution were first reported by Kirk *et al.*,[1] then by Shih *et al.*,[2] and many others.[3,4] The topographical features observed in these works are qualitatively consistent, although the conclusion of the "missing Bi-atom row" drawn by Kirk *et al.* has been questioned. A detailed analysis[2] reveals that the corrugations observed in these images agree very well with the lattice structure of the BiO plane in the bulk derived from x-ray diffraction.[5] This confirms that the cleavage plane of the 2:2:1:2 compound is the BiO plane. However, many more questions remain. For example, in the STM images, one only observes a single corrugation feature associated with each lattice point, whereas there are two atoms, one Bi and one O, associated with each lattice point. The following question arises: Do these corrugation maxima correspond to the atomic positions of Bi or O, or to something else? In the case of GaAs(110) 1×1 and Si(111) 2×1 surfaces, similar questions have been resolved by the technique of polarity-dependent imaging combined with extensive spectroscopic studies.[6,7] In those two cases, the images at opposite polarities show complimentary corrugations which are related to surface electronic structures. In order to correctly interpret STM images in the 2:2:1:2 compounds, a similar investigation is needed. However, the problem in this case is more difficult since the geometric structure is more complicated and the electronic structure is poorly understood.

Spectroscopy of Bi-Sr-Ca-Cu-O 2:2:1:2 has shown that the surface BiO layer is nonmetallic, as first reported by us.[2] Similar results were reported independently by Tanaka *et al.*,[8] and more recently by Wu *et al.*[4] Furthermore, Hasegawa *et al.*[9] have performed cross-sectional STM studies of the *b*-*c* and *a*-*c* planes of 2:2:1:2 compounds and also reported that the BiO layer in the bulk is nonmetallic. These results disagree with band-structure calculations,[10] which predict a metallic BiO band. On the other hand, Olson *et al.*[11] used angle-resolved photoemission spectroscopy to study the cleaved 2:2:1:2 compound and reported that the E versus $\mathbf{k}$ dispersion relationship of the BiO band intersects the Fermi level at the same k position as the band calculation predicts. We note that Wells *et al.*[12] have found that the surface BiO band can be either metallic or nonmetallic depending on the oxygen-annealing process. Thus, unless the 2:2:1:2 compounds studied in these STM works[2,4,8,9] all have similar stoichiometry to the nonmetallic one reported by Wells *et al.*,[12] then the results of STM spectroscopy disagree with those of angle-resolved photoemission spectroscopy.[11]

In photoemission, the spectrum represents an average of 10–20 Å in depth, and the separation of the contributions from different layers is nontrivial. In STM, usually only the electronic states on the surface layer contribute to the tunneling process. If the surface layer is metallic, then the electronic states in this layer make the dominant contribution to the tunneling current. However, if the surface layer has a band gap and the underlying layer is metallic, then, when the sample bias puts the Fermi level of the tip within the band gap of the surface layer, the underlying layer is primarily responsible for the tunneling. An alternative way of viewing this phenomenon is that the wave functions of the underlying states can tail into the band-gap region of the surface layer, thus forming a residual density of states at the surface. The question one needs to answer is whether or not these states are detectable and how they compare to those of a typical metallic surface. A practical concern, which is important for the measurement of the superconducting gap, is whether one can tunnel into the states near the Fermi level without crashing the tip into the sample.

The objective of our work is a better understanding of the atomic arrangement and the electronic properties of these 2:2:1:2 compounds. We report topographic STM images obtained simultaneously at different voltages, spectroscopic results obtained at different stabilization voltages, and the corresponding junction characteristics. We also obtain the absolute tip-to-sample distance as a function of sample bias, and relate this result to the junction characteristics. Finally, we report an observation of the field penetration into the sample, which can occur only if the surface layer is not metallic.

II. EXPERIMENT

The experimental setup for our STM has been described previously.[13] Single crystals of Bi-Sr-Ca-Cu-O samples with a T_c onset of 84 or 91 K were cleaved in an ultrahigh-vacuum chamber with base pressure of $<4\times10^{-11}$ Torr, exposing the *a*-*b* plane. Tungsten tips, cleaned *in situ* by electron-bombardment heating, were used. All the studies were performed at room tempera-

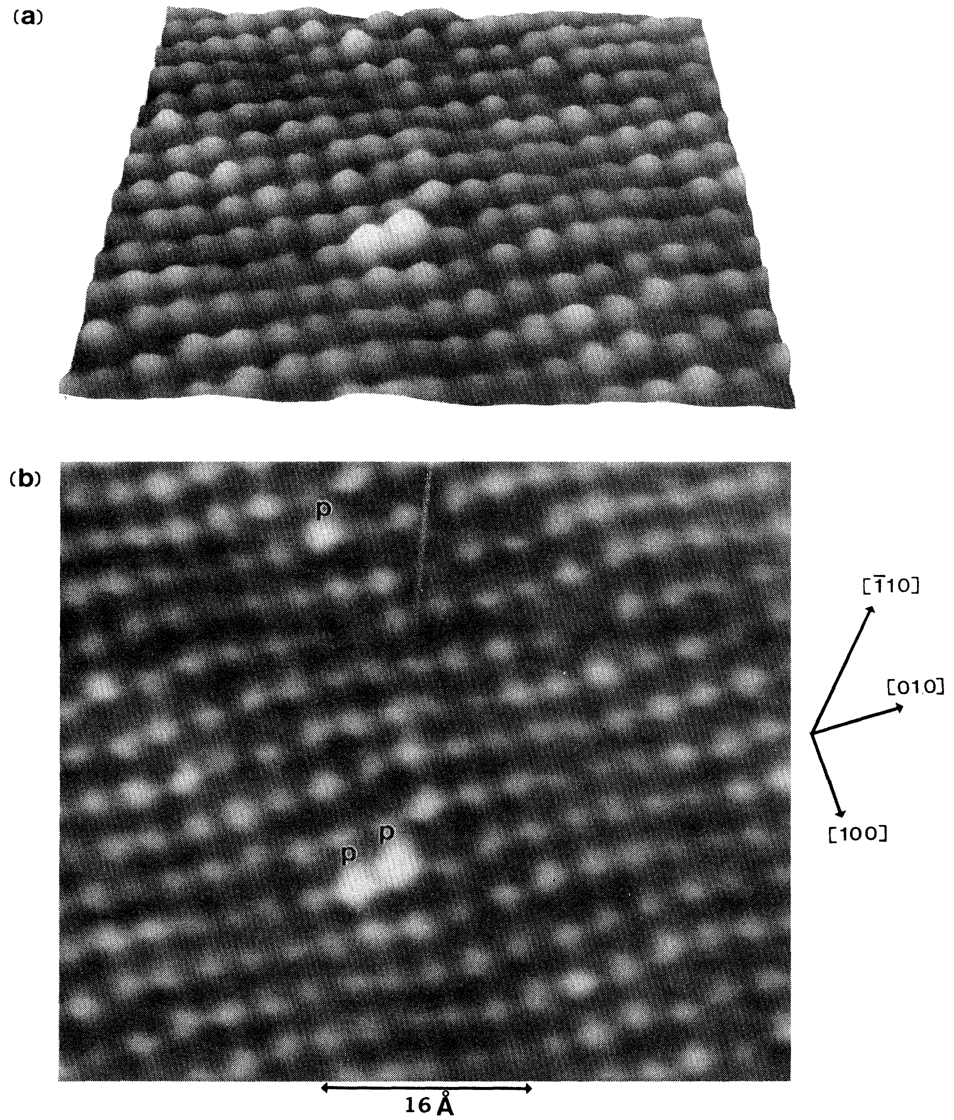

FIG. 1. (a) Perspective view and (b) top view of a STM image taken at a sample bias of −0.75 V. The pervoskite axes are labeled as [100] and [010], and the incommensurate superstructure direction **b** is labeled as [$\bar{1}$10]. The protrusions are labeled as *P*.

ture. Low-energy electron diffraction (LEED) was performed either before or after STM studies to determine the surface orientation. STM images were acquired at a constant current of 100 pA. Spectroscopic data were taken by interrupting the feedback loop used for topographic imaging: the tip-to-sample separation was decreased as the sample bias was reduced in order to establish a large dynamic range, and the conductivity was measured using a lockin amplifier.

III. RESULTS AND DISCUSSION

A. Topography, polarity-dependent images

In Figs. 1(a) and 1(b), we show the perspective and top views of an STM image taken at a sample bias of -0.75 V. While the in-plane sinusoidal modulation is clearly observed in the top view (e.g., by viewing Fig. 1 from the side), the out-of-plane modulation is more clear in the perspective view. We use the same crystallographic notations as a previous publication,[2] where the perovskite axes are labeled as [100] and [010], and the incommensurate superstructure direction **b** is labeled as $[\bar{1}10]$. The modulation amplitude and periodicity are identical to those found in our previous paper,[2] except that the image shown here has a better signal-to-noise ratio. The protrusions (labeled as *P*) shown in the image are likely due to substitutional defects, since the corrugation maxima coincide with the rest of the image. As before, we do not observe the "missing atom row" in these high-quality images. However, depending on the sample bias, we have occasionally observed atomic rows depressed downward (but not missing atoms). Figure 2 shows one example. The depressed atomic rows are marked by the long arrows. Double-tip effects are not likely to exist in this image since single-atom protrusions (labeled as *P*) are clearly observed.

As we described in the Introduction, there is one Bi and one O associated with each lattice point. However, we only observe one corrugation maximum per lattice point. To better understand what the corrugation maxima correspond to, we also performed polarity-dependent imaging similar to that used for GaAs(110) and Si(111) 2×1 surfaces.[6,7] Figures 3(a) and 3(b) show STM images simultaneously taken at sample biases of -1.75 and 1.75 V, respectively. The crosshairs are located in identical locations in both images. A close examination reveals that the corrugations in these two images are in phase. Similar polarity-dependent measurements performed at bias range from ±0.5 to ±1.50 V show the same result.

This result of in-phase corrugations between opposite polarities was a surprise to us. Based on the spectroscopic studies, which will be discussed in more detail, the surface BiO layer is nonmetallic. Intuitively, one would think that this result is due to the ionic nature of the Bi-O bond; thus, one would expect to see that the images of occupied states and unoccupied states should show complimentary corrugations, as do those of the GaAs(110) surface.[6] We note that, according to the band calculations, the states near the Fermi level (both occupied and unoccupied states) are primarily Bi derived, which is consistent with a result of "in-phase corrugations between opposite polarities." However, these calculations also predict a metallic BiO band which does not agree with our spectroscopic studies. We will discuss possible explanations for this result of in-phase corrugations be-

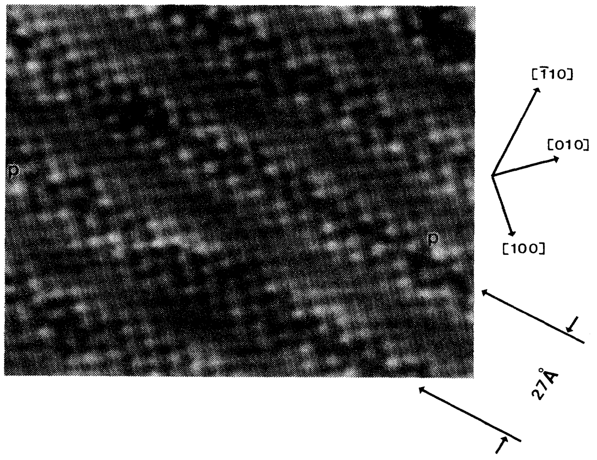

FIG. 2. Top view of a STM image taken at a sample bias of -1.25 V. The depressed atomic rows are marked by the long arrows. Single-atom protrusions are labeled as *P*.

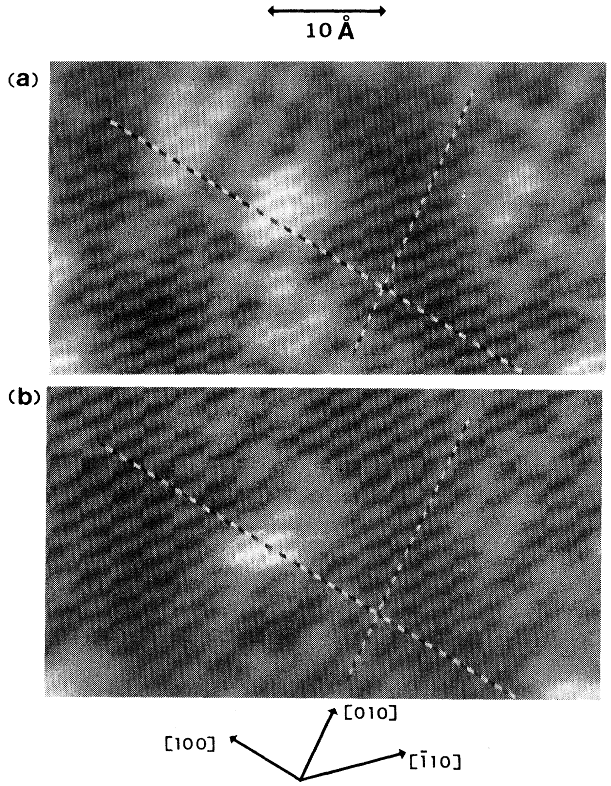

FIG. 3. STM images recorded simultaneously at (a) -1.75 and (b) 1.75 V. The crosshairs are located in identical locations in both images.

tween opposite polarities further, after the discussion of the spectroscopic studies.

B. Spectroscopy, junction characteristics, and the absolute tip-to-sample distance

For our spectroscopic studies, we use a method which yields a high dynamic range in the measurement of current and conductivity, as previously described.[14] We obtain this high dynamic range by varying the tip-to-sample separation s as a function of bias voltage V between tip and sample. The conductivity is then normalized to a constant-s value which is independent of the $s(V)$ contour used in the measurement. Furthermore, the decay constant κ of the tunneling probability within the $s(V)$ contour is also obtained. This $\kappa(s(V))$, which characterizes the tunneling junction, is very important for appropriate interpretations of the spectroscopic results. Details of this method can be found in the Appendix.

Figure 4 shows constant-s conductivities of cleaved 2:2:1:2 samples measured in various experiments. These spectra were taken when stable STM images were also obtained either before and after, or during the acquisition of tunneling spectra. We found that the spectra showed little spatial dependence within the experiment. The spectra are displaced vertically for clarity. Thus, the scale is not an absolute scale for all spectra, instead, it only shows the relative scale within each spectrum. Also shown on the top is a spectrum taken on a β-Sn film deposited on a GaAs substrate, for a metallic reference. In these spectra, the sample bias at which each tunnel junction was initially stabilized, V_{stab}, is marked with an asterisk. Presumably, the larger V_{stab} is, the further away the tip is. In spectra which span a larger range of sample biases (a) and (b), we observe a sharp rise of the conductivity at 1.5 eV above and below the Fermi level (i.e., 0-V sample bias), forming a "quasigap" of about 2.5–3 eV. Within this quasigap, various spectral features can also be observed. In Fig. 4, curve (a), negative differential conductivity is observed between 1.5 and 1.9 V, and is shown as a dotted curve. Although Fig. 4, curves (a) and (b) have high dynamic ranges of 4–6 orders of magnitude, we could not detect conductivity for sample bias near zero. If we compare these two spectra with the constant-s spectrum for a metal shown on the top (since they are at similar V_{stab}), which shows a range of only 1.5 orders of magnitude from -2.5 to 2.75 V, we can conclude that the surface density of states at the Fermi level is *at least* 3–4 orders of magnitude smaller than that of a normal metal.

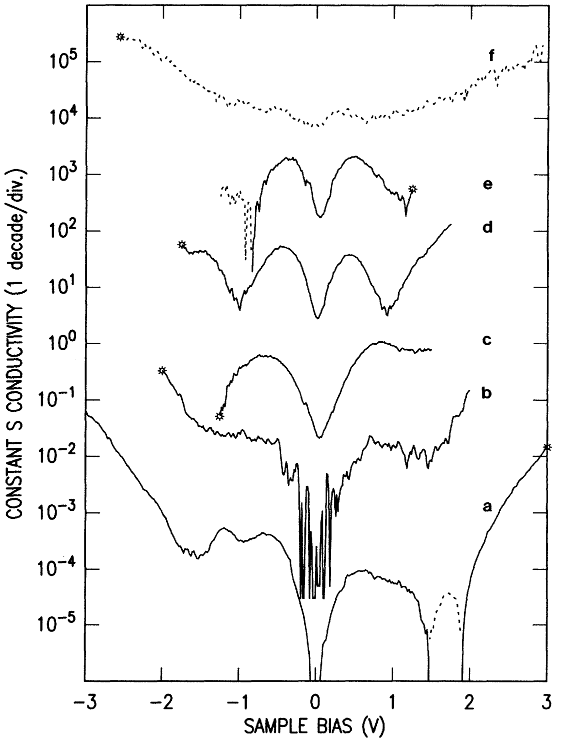

FIG. 4. Constant-s conductivities of cleaved 2:2:1:2 samples measured in various experiments (a)–(e), and that of a β-Sn film deposited on a GaAs substrate (f). The Fermi level corresponds to a 0-V sample bias. The sample bias at which each tunnel junction was initially stabilized, V_{stab} is marked with an asterisk. The spectra are arbitrarily displaced vertically for clarity. Thus, the scale only shows the relative magnitude within each spectrum. When the signal is too small to be detected, it appears as a glitchy noise in a logarithmic scale such as that shown in (b) near zero bias. In (b), the cutoff is arbitrarily set at 3×10^{-5}. A similar noise will appear in (a) if the cutoff is set lower.

The spectra shown in Fig. 4, curves (a) and (b) were taken when the tunneling junction was initially stabilized at a relatively large V_{stab} of 3 and -2.25 V. In Fig. 4, curves (c)–(e), we show spectra taken at smaller V_{stab} of -1.2, -1.7, and 1.2 V, respectively. These stabilization voltages lie either within or on the edge of the "quasigap." In these spectra one can observe small but nonzero conductivities for sample biases near zero (a factor of 30 smaller than the conductivity at 0.5 V), although the voltage dependence is extremely nonlinear. Spectra taken at even lower stabilization voltages (<1.0 V) also show very similar structure. Also shown as a dotted curve in Fig. 4, curve (e) is a negative conductivity region. The spectral features of these spectra taken at low V_{stab} are consistent with the spectral features in the "quasigap" of the spectra taken at higher V_{stab} except for the detectability of the conductivity near zero bias. However, one can still safely conclude that the surface density of states at the Fermi levels is very small. The origin of the zero-bias conductivity is discussed below.

In order to appropriately interpret the spectroscopic results, we have investigated the junction characteristics. Figures 5(a)–5(c) show the raw I-V, σ-V, and s-V curves which are used to deduce the constant-s spectrum shown in Fig. 4, curve (a). Note that the tip-to-sample distance shown in Fig. 5(c), and the distance shown in Fig. 6, is relative to the smallest distance in each measurement, instead of the absolute s value. The absolute s value will be discussed later. As mentioned above, the decay constant for the tunneling probability in the measurement $\kappa(s(V))$ can also be deduced. In Fig. 6, curve (a), we show, for the data of Fig. 5, the ratio of the conductivity at constant s, σ_s, relative to the measured conductivity σ_m, as a function of the relative tip-to-sample separation. The slope in this plot reflects the decay constant κ as a function of relative tip-to-sample separation. The open circles are data points for the negative sample bias (filled states) and the solid circles are those for the empty states. The average barrier height for the junction at large s is about 4 eV ($\kappa \approx 1$ Å^{-1}), consistent with vacuum tunneling behavior. As s decreases by about 2 Å, the barrier height decreases drastically (<0.5 eV). The low-barrier-height region corresponds to the "quasigap" region in spectra Fig. 4, curve (*a*), which can be easily inferred from the *s*-*V* contour shown in Fig. 5(c). Similarly, for the spectrum taken at a low stabilization voltage of 1.2 V, corresponding to Fig. 4, curve (*e*), we observed a low barrier height of 1.4 eV which is shown in Fig. 6, curve (*b*). This result indicates that the tunnel junction stabilized at a low voltage is *not* a normal vacuum-tunneling junction. More likely, the tip is nearly in direct contact with the sample.

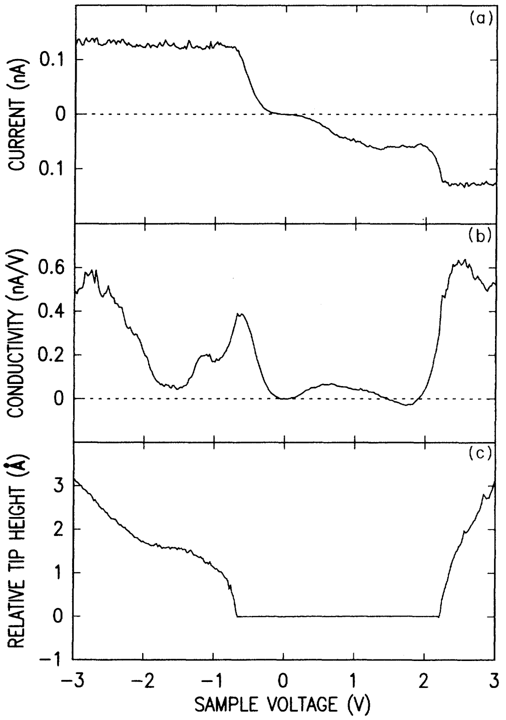

FIG. 5. Raw data for (a) the tunneling current, (b) the conductivity, and (c) the applied variation in tip-to-sample separation, as a function of sample voltage obtained from a cleaved 2:2:1:2 sample. These curves are used to deduce the constant-*s* conductivity shown in Fig. 4, curve (*a*).

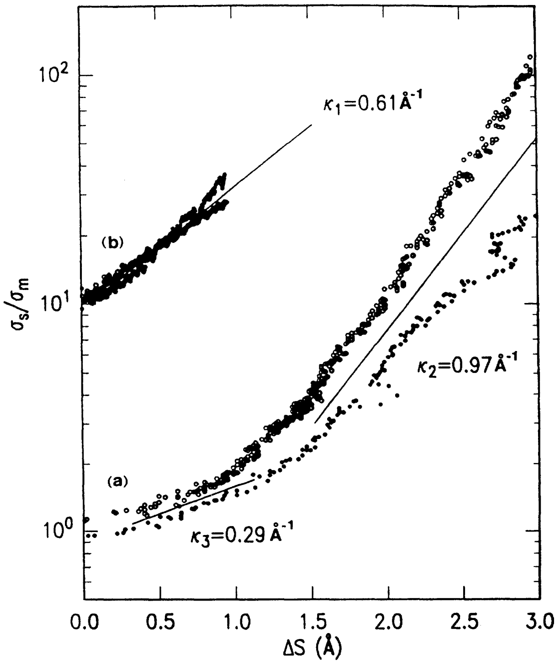

FIG. 6. The ratio of the conductivity at constant s, σ_s, relative to the measured conductivity σ_m, as a function of the relative tip-to-sample separation. Curve (*a*) corresponds to the measurement for the spectrum shown in Fig. 4, curve (*a*), and curve (*b*) corresponds to that shown in Fig. 4, curve (*e*). The open circles are data points for the negative sample bias (filled states), and the solid circles are those for the empty states. Small values of Δs refer to voltages near 0 V in Fig. 4.

In order to understand this fast change of junction characteristics as a function of s, we have investigated the absolute tip-to-sample separation using the technique of vacuum resonance tunneling.[15] Figure 7 shows the experimental data of constant-current conductivity and tip-to-sample distance as solid curves, and those of the theoretical fitting for a free-electron system are shown as dashed curves. The experimental data are taken at constant current of 1×10^{-10} A. The fitting parameters are a work function of 4.15 eV, a current density of 2.7×10^{-12} A/Å^2, and the radius of the curvature of the tip of 25 Å. The first oscillation of the resonance tunneling predicted by the free-electron model was not observed in the experimental data. We attribute this result to the interference of the spectral features in the unoccupied states of the sample. The absolute tip-to-sample separation is determined by matching the experimental and theoretical $s(V)$ curves, as shown in the lower part of Fig. 7. At a bias of 2 V and a tunneling current of 100 pA, the tip-to-sample separation is only 6 Å. A similar measurement performed on a *p*-type GaAs(110) surface shows that s is about 12 Å at a 2-V sample bias (only 0.6 eV above the conduction-band minimum). Furthermore, in GaAs at an s value of 10 Å, one has no difficulty detecting states near the band edges. The smaller absolute tip-to-sample separation at low bias in the Ba-Sr-Ca-Cu-O 2:2:1:2 compound is consistent with the spectroscopic finding of a very low density of states near the Fermi level.

Because of the complicated layered structure of 2:2:1:2 compounds, the small s at low sample bias has very important consequences for the interpretation of the STM images and the spectroscopic results. Firstly, we note that the average distance between CuO and BiO layers is only 4.5 Å. Thus, as s is decreased and the tunneling barrier height decreases rapidly, the states originating from the CuO layer can make substantial contributions to the spectral features observed within the "quasigap." We neglect the contribution from the SrO layer since this layer is insulating. For instance, in spectra such as that shown in Fig. 4, curve (*e*), the observed finite conductivity at zero bias likely results from the states originating from CuO. However, there is also the possibility that the surface electronic structure is strongly modified due to the tip-to-sample interaction at small *s*. In any case, the small value of *s* required for 100-pA tunneling current at biases of less than 2 V makes it clear that the surface BiO layer is nonmetallic.

As a result of the nonmetallic surface BiO layer, when *s* is decreased, there is a possibility of field penetration into the sample up to the CuO layer, since the surface density of states near the Fermi level is too low to screen the electrical field. We assume that the density of states in the CuO layer at the Fermi level is high enough to screen the field completely, and prevent further field penetration. This field penetration further reduces the voltage drop between the BiO layer and the tip, thus reducing the contribution to the tunneling current from the BiO layer. In the extreme case where the tip touches the BiO layer, all of the voltage drop occurs between the BiO and CuO layers. The experimental evidence for field penetration is discussed below.

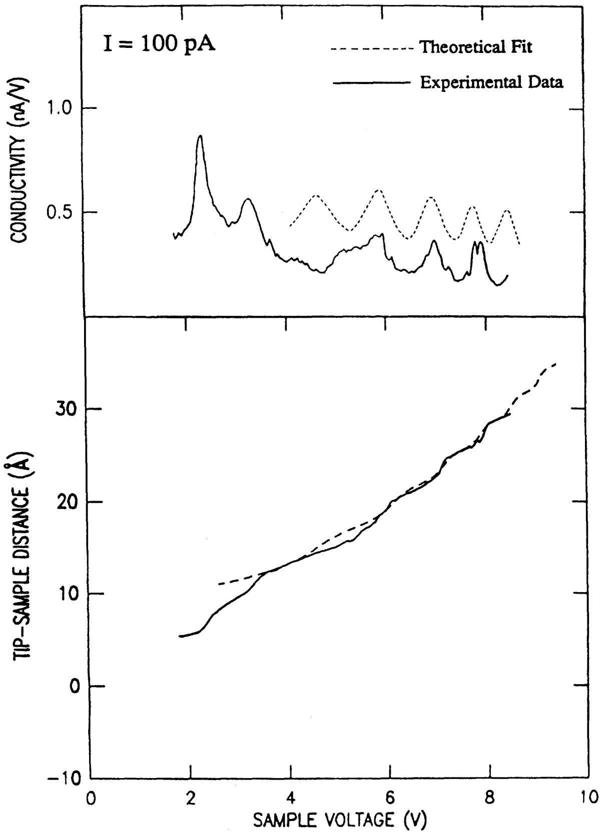

FIG. 7. The experimental data of constant-current conductivity and tip-to-sample distance (shown as solid curves), and those of the theoretical fitting for a free-electron system (shown as dashed curves). The experimental data is taken at constant current of 1×10^{-10} A. The fitting parameters are a work function of 4.15 eV, a current density of 2.7×10^{-12} A/Å^2, and the radius of the curvature of the tip of 25 Å. The theoretical fitting of the conductivity is normalized to a tunneling current of 100 pA, and for ease of viewing is shifted upward by 0.25 nA/V. Except for the first oscillation in the resonance tunneling region, the oscillation periodicity and amplitude in both the conductivity and tip-to-sample distance show good agreement between the theory and experiment.

C. Field penetration

Figure 8 shows two constant-current conductivities measured as a function of sample bias. Note that the vertical scale of spectrum (*a*) is a factor of 2 smaller than that of spectrum (*b*). Before the spectrum (*a*) was taken, the tunnel junction was stabilized at a 1.25-V sample bias, at which many spectra similar to Fig. 4, curve (*e*) and good atomic images had been obtained. In this spectrum, one does not observe vacuum resonances above 4 V. We attribute this absence of the resonances to the field penetration into the sample, which causes the voltage drop across the BiO layer and the tip to be less than the sample bias. After a few similar measurements which yielded spectra such as Fig. 8, curve (*a*), the surface spontaneously relaxed to a configuration which was free of the field penetration. However, the cause of the relaxation of the field penetration cannot yet be identified. In the latter configuration, we observed spectra such as (*b*) which showed the oscillation in the conductivity due to the resonance tunneling through the vacuum barrier. If one closely examines spectra (*a*) and (*b*), one finds very similar structures below the onset of the barrier resonance, although these structures are at different bias positions. As mentioned previously, in spectrum (*a*) the voltage drop across the BiO layer and the tip is less than the sample bias, which accounts for this voltage lag. Furthermore, as both of these spectra were taken using a lock-in amplifier with the sample amplitude of modulation voltage, if one considers that the field penetration reduces

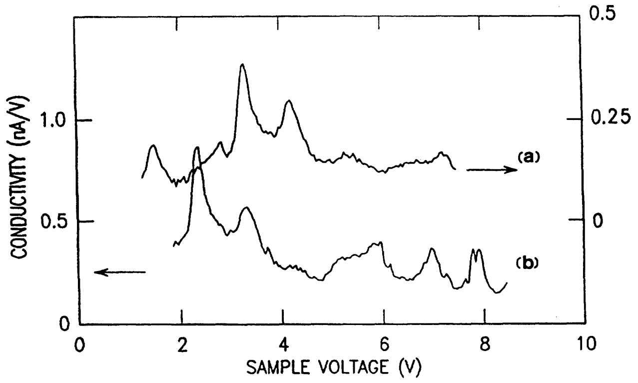

FIG. 8. Constant-current conductivities measured as a function of sample bias at a constant current of 100 pA. Note that the vertical scale of spectrum (*a*) is a factor of 2 smaller than that of spectrum (*b*).

the amplitude of the effective modulation voltage between the tip and the BiO layer, then the smaller magnitude in the conductivity observed in spectrum (*a*) is also accounted for.

We now present a simple model to describe the effects of field penetration more quantitatively. Figure 9 shows a schematic of this model. V_b is the voltage between the tip and the surface BiO layer (subscript b stands for the voltage drops on the BiO layer), V_p is the voltage between the BiO and CuO layers (subscript p stands for the penetration voltage), then the sample bias $V_s = V_b + V_p$. The distance between the BiO layer and the tip is $S(V_b)$. We take the distance between the BiO and CuO layers to be the average value, $d_0 = 4.5$ Å. Furthermore, we assume a constant dc dielectric constant ϵ between the BiO and CuO layers. The boundary condition for field penetration is

$$\epsilon V_p / d_0 = V_b / S(V_b) \; .$$

From this boundary condition and $V_s = V_b + V_p$, we can derive a simple relation between the voltages with and without field penetration:

$$V_s = V_b[1 + d_0/\epsilon S(V_b)] \; .$$

By using the absolute tip-to-sample distance $S(V_b)$ determined from the vacuum resonances, and choosing an ϵ value of 1.4 for the best fit, we can simulate the effect of field penetration, thus converting the spectrum without field penetration, Fig. 8, curve (*b*), into a rescaled spectrum Fig. 10, curve (*b*). The rescaled spectrum, Fig. 10, curve (*b*), shows excellent agreement with the spectrum 8, curve (*a*) [now shown as Fig. 10, curve (*a*)], except that the peak at 7 V is slightly off. Although the detailed mechanism for the onset and relaxation of field penetration is still not clear, this comparison unambiguously shows that spectrum 8, curve (*a*) involves field penetration into the sample. Again, field penetration can happen only if the surface BiO layer is not metallic.

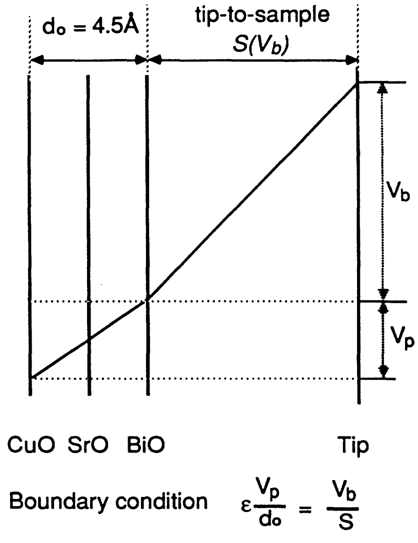

FIG. 9. Schematic of a simple field-penetration model. V_b is the voltage between the tip and the surface BiO layer (subscript b stands for the voltage drops on the BiO layer), V_p is the voltage between the BiO and CuO layers (subscript p stands for the penetration voltage). The sample bias $V_s = V_b + V_p$. $S(V_b)$ is the separation between the BiO layer and the tip. The distance between the BiO and CuO layers is d_0. The dc dielectric constant is ϵ.

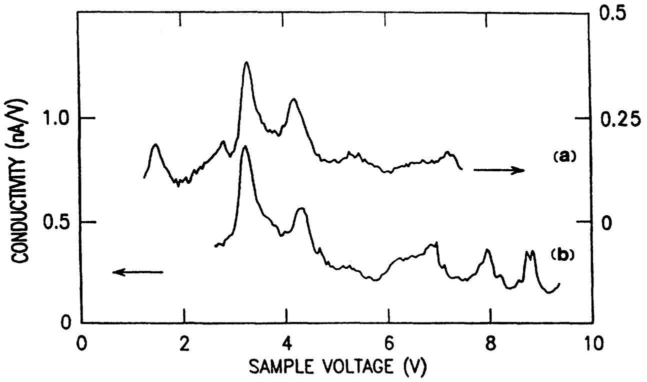

FIG. 10. Constant-current conductivity spectra of (*a*) reproduction of Fig. 8, curve (*a*), and (*b*) a rescaled spectrum of Fig. 8, curve (*b*) using the simple field-penetration model shown in Fig. 9.

D. Possible explanations for polarity-dependent images

We now return to the discussion of polarity-dependent images shown in Fig. 2 which show in-phase corrugations between the images obtained at opposite polarities. In our experiments, atomic images are usually obtained at low sample biases (<2 V), especially if simultaneous imaging at different polarities is to be achieved. As we discussed in the spectroscopy section, at these biases, the tip-to-sample separation is between 3 and 6 Å, which is much smaller than usual. Furthermore, there is also the likelihood of field penetration into the sample. As a result, there may be appreciable contributions to the tunneling current from states in the CuO layer. However, the observed corrugation is consistent with the topographic features of the BiO layer instead of the CuO layer. One possible explanation is that the observed corrugations are due to fluctuations in the local barrier height which reflect the lattice arrangement of the surface BiO layer. This would explain the in-phase corrugations between the images obtained at opposite polarities. A more detailed investigation is needed to verify this interpretation. For instance, one should simultaneously perform the polarity-dependent topography and barrier-height imaging.

There are other alternative explanations. One of them is that the occupied and unoccupied states within ±1.5 eV of the Fermi level are all derived from the same chemical element, which could be either Bi or O. According to the band calculations, states near the Fermi level are Bi derived, and the BiO layer is metallic. This result was used by Kirk *et al.*[1] to interpret their images. Although this can explain the in-phase corrugations between opposite polarities, it is not consistent with the nonmetallic property of the surface BiO layer in our study. Furthermore, as we have discussed in a previous paper,[2] there is evidence from other studies that the states near the Fermi level are oxygen derived. Nevertheless, it is still possible that the superstructure modulation causes the gap opening in the otherwise metallic BiO band.

Another explanation is related to the very small tip-to-sample distance. As has been discussed by many others in explaining the STM images observed in graphite,[16] the small tip-to-sample distance causes a strong interaction between the tip and sample. As a result, the tunneling barrier collapses, and new states can be induced. The lowering of the tunneling barrier is certainly observed in our experiment. The open question is whether new states are induced by the tip-to-sample interaction, which are responsible for the phase relation between the corrugations taken at opposite polarities and consistent with the observed tunneling spectroscopy.

IV. SUMMARY

In summary, we have used scanning tunneling microscopy and spectroscopy to study the topographic and electronic properties of the Bi-Sr-Ca-Cu-O 2:2:1:2 compounds. Voltage-dependent images show that the corrugations between images taken at opposite polarities are in phase. Spectroscopic studies show that the surface density of states at the Fermi level is very small (about 3–4 orders of magnitude less than a typical metal). Finite conductivity at zero bias is detectable at low stabilization voltages and very small tip-to-sample distances (3–6 Å). At these small tip-to-sample distances, the tunneling barrier height (<1.5 eV) is substantially smaller than that of a vacuum-tunneling junction. The detected finite conductivity may result from a very low state density in the surface BiO layer or it may come from the underlying CuO layer. We also observe a phenomenon of "field-penetration" into the sample, consistent with a nonmetallic surface BiO layer.

ACKNOWLEDGMENTS

We thank J. R. Kirtley and W. Shaffer for valuable discussions during the course of this work.

APPENDIX

For our spectroscopic studies with the STM, we use a method which yields a high dynamic range in the measurement of current and conductivity, as previously described.[14] This method is principally useful for systems which display a surface-state band gap, in which case conductivity measurements over many orders of magnitude are required to properly define the band edges and probe the gap region for the existence of states. We obtain this high dynamic range by varying the tip-to-sample separation s as a function of bias voltage between tip and sample V. An analysis method then provides a parameter-free transformation from conductivity measured with any arbitrary $s(V)$ contour to conductivity at constant tip-sample separation. This analysis method is described here, and we examine the validity of the approximations made in the derivation of the method.

The input to the analysis method consists of a measurement of the current $I_m(s(V),V)$ and the conductivity

$$\sigma_m(s(V),V) \equiv \partial I_m/\partial V|_s ,$$

where, at each V, the derivative is measured at a *fixed* tip-to-sample separation. The subscript m denotes the *measured* quantity. The relative tip-to-sample separation $s(V)$ used for the measurement is also known. Our analysis method is based on the use of the logarithmic derivative

$$g_m(s(V),V) \equiv \sigma_m(s(V),V)/I_m(s(V),V) .$$

Since the logarithmic derivative equals the *ratio* of conductivity to current, it is approximately independent of the tip-to-sample separation for small changes in the separation. Denoting the logarithmic derivative at some constant-s value of $s=s'$ to be $g(s',V)$, we have

$$g(s',V) \simeq g_m(s(V),V) . \tag{A1}$$

This is the only approximation made in our analysis, and we examine its validity below. Now, from the definition of $g(s',V)$, we have

$$g(s',V) \equiv \frac{\sigma(s',V)}{I(s',V)} = \frac{d}{dV}\ln I(s',V) \tag{A2}$$

(note that the total derivative on the right-hand side of this equation is valid only since the current is evaluated at constant $s=s'$). From Eq. (2) it follows that

$$\frac{I(s',V)}{I(s',V')} = \exp\left[\int_{V'}^{V} g(s',E)dE\right] \tag{A3}$$

for any V and V' which have the same sign. Differentiating with respect to V then yields

$$\sigma(s',V) = I(s',V')g(s',V)\exp\left[\int_{V'}^{V} g(s',E)dE\right] . \tag{A4}$$

This equation gives the conductivity at any value of s, in particular, at $s=s'$. The value of V' is arbitrary; the choice of a different V' simply introduces a scale factor multiplying the exponential term which is cancelled by the $I(s',V')$ multiplier as seen from Eq. (A3).

Equation (A4) provides the conductivity at a constant tip-to-sample separation, which is the desired result of our analysis. To evaluate this equation in terms of the measured data, we use Eq. (A1) to evaluate the logarithmic derivative. Furthermore, we evaluate the term $I(s',V')$ from the measured quantity $I_m(s(V'),V)$, in which case it is necessary to take $s'=s(V')$. The evaluation of Eq. (A4) in terms of measured quantities is then given by

$$\sigma(s',V) = I_m(s(V'),V')g_m(s(V),V) \times\exp\left[\int_{V'}^{V} g_m(s(E),E)dE\right] . \tag{A5}$$

We write Eq. (A5) using an equals sign, since it now serves as the definition of $\sigma(s',V)$ as obtained from our analysis method. We bear in mind, however, that $\sigma(s',V)$

thus obtained may differ from the actual conductivity due to the use of Eq. (A1), and we return to examine this difference below. Using Eq. (A5), we evaluate the conductivity at a constant tip-to-sample separation, as shown in Fig. 4 of this paper. Furthermore, we consider the ratio of the constant-s conductivity to the measured conductivity, as shown in Fig. 6. From Eq. (A5), this quantity is given explicitly by

$$\frac{\sigma(s',V)}{\sigma_m(s(V),V)}=\frac{I_m(s(V'),V')}{I_m(s(V),V)}\exp\left[\int_{V'}^{V} g_m(s(E),E)\,dE\right] . \tag{A6}$$

We now wish to evaluate the dependence of the conductivity on the tip-to-sample separation, as done in Fig. 6, by measuring the slope of

$$\sigma(s',V)/\sigma_m(s(V),V)$$

as a function of s, on a logarithmic scale. Defining that slope to be $2\tilde{\kappa}$, the measurement of the decay constant $\tilde{\kappa}$ can then be written as

$$\tilde{\kappa}=\frac{1}{2}\frac{d}{ds}\ln\left[\frac{\sigma(s',V)}{\sigma_m(s(V),V)}\right] . \tag{A7}$$

Combining Eqs. (A6) and (A7) we have, for measured $\tilde{\kappa}$,

$$\tilde{\kappa}=\frac{1}{2}\frac{d}{ds}\left[\ln\left[\frac{I_m(s(V'),V')}{I_m(s(V),V)}\right]+\int_{V'}^{V} g_m(s(E),E)\,dE\right] . \tag{A8}$$

Due to the use of the approximate equation (A1), the values of the decay constant $\tilde{\kappa}$ obtained from Eq. (A8) may differ from the actual decay constant. To evaluate this difference, we consider an explicit form for the actual (i.e., measured) current,

$$I_m(s,V)=I_0(V)\exp[-2\kappa(s,V)s(V)] , \tag{A9}$$

where we take the actual decay constant $\kappa(s,V)$ to be a completely general function of s and V. From Eq. (A9), the logarithmic derivative is found to be

$$g_m(s,V)=\frac{\sigma_0(V)}{I_0(V)}-2s(V)\left.\frac{\partial\kappa(s,V)}{\partial V}\right|_s , \tag{A10}$$

where $\sigma_0(V)\equiv dI_0(V)/dV$. Substituting Eqs. (A9) and (A10) into Eq. (A8), we find, after some manipulations, that

$$\tilde{\kappa}=\kappa(s,V)+s(V)\left.\frac{\partial\kappa(s,V)}{\partial s}\right|_V . \tag{A11}$$

Equation (A11) is a major result of this appendix. It expresses the relationship between the true decay constant $\kappa(s,V)$ and the measured decay constant $\tilde{\kappa}$, which is obtained using the analysis method described above. Upon consideration of the right-hand side of Eq. (A11), we see that it can be rewritten in terms of the general form of $I_m(s,V)$, Eq. (A9), with

$$-\frac{1}{2}\left.\frac{\partial\ln I_m(s,V)}{\partial s}\right|_V=\kappa(s,V)+s(V)\left.\frac{\partial\kappa(s,V)}{\partial s}\right|_V , \tag{A12}$$

so that

$$\tilde{\kappa}=-\frac{1}{2}\left.\frac{\partial\ln I_m(s,V)}{\partial s}\right|_V . \tag{A13}$$

The right-hand side of Eq. (A13) is the quantity which is conventionally used to directly measure the decay constant.[17,18] Thus, we conclude that the decay constant $\tilde{\kappa}$ obtained from our analysis method is identical to that which is conventionally measured.

Let us now consider the values of the constant-s conductivity $\sigma(s',V)$ obtained from our analysis method. Due to the use of the approximate equation (A1), these may differ from the actual values $\sigma_m(s',V)$. To obtain a formula for this difference, we integrate Eq. (A7) from s' to s, and combine it with the expression for $\sigma_m(s',V)$ obtained by differentiating Eq. (A9), yielding

$$\frac{\sigma(s',V)}{\sigma_m(s',V)}=f(V)\exp\left[2\int_{s'}^{s}\tilde{\kappa}\,ds-2\kappa(s,V)s(V)+2\kappa(s',V)s'\right] , \tag{A14}$$

where the prefactor $f(V)$ is given by

$$f(V)=\frac{\sigma_0(V)-2I_0(V)s(V)[\partial\kappa(s(V),V)/\partial V]|_s}{\sigma_0(V)-2I_0(V)s'[d\kappa(s',V)/dV]} \tag{A15}$$

with $\sigma_0(V)\equiv dI_0(V)/dV$. Equation (A14) can be rewritten by using Eq. (A11) for $\tilde{\kappa}$ which, after some manipulations, yields

$$\frac{\sigma(s',V)}{\sigma_m(s',V)}=f(V)\exp\left[-2\int_{V'}^{V}\left[s(E)\left.\frac{\partial\kappa(s(E),E)}{\partial E}\right|_s-s'\frac{d\kappa(s',E)}{dE}\right]dE\right] \tag{A16}$$

with $f(V)$ given by Eq. (A15). We see from these equations that the accuracy of our determination of $\sigma(s',V)$ is determined mainly by the derivative with respect to voltage of the decay constant. The magnitude of this effect can be best understood by considering a numerical example.

As a numerical example, we consider solutions for tunneling between metal electrodes, using a trapezoidal barrier including an image potential term, and where the tunnel current is computed by numerical integration of Schrödinger's equation.[19] We take the work function of both electrodes to be $\phi=4.4$ eV, so that the ideal value of the decay constant is

$$\kappa_0=\sqrt{(2m\phi)}/\hbar=1.07\ \text{Å}^{-1} .$$

Given the tunnel current and its derivatives, we compute $\kappa(s,V)$ from Eq. (A9), and $\tilde{\kappa}$ from Eq. (A11) or (A13). The results are shown in Fig. 11, for a bias voltage of $V=1$ V. We see that the reduction of the tunnel barrier

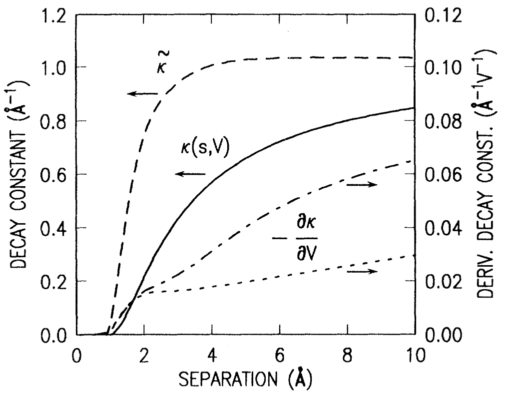

FIG. 11. Simulated values for the actual decay constant $\kappa(s,V)$ (solid line), and the measured decay constant $\tilde{\kappa}$ (dashed line) obtained using the analysis method described in the text at a tip-to-sample bias voltage of 1 V. Results for the derivative of the decay constant $-\partial\kappa(s,V)/\partial V|_s$ are also shown at bias voltages of 1 (lower, dotted line) and 3 V (upper, dot-dashed line).

due to the image potential shows up clearly in $\kappa(s,V)$, whereas it cancels out to lowest order in $\tilde{\kappa}$, as discussed by Binnig *et al.*[18] Also shown in Fig. 11 are values for the derivative $\partial\kappa(s,V)/\partial V|_s$, at bias voltages of 1 and 3 V. At larger voltages and separations, the magnitude of this derivative is always less than $\kappa_0/(2\phi)=0.12$ Å^{-1}V^{-1}.

Using the numerical results of the above example, we numerically compute the ratio of $\sigma(s',V)/\sigma_m(s',V)$ from Eqs. (A15) and (A16), which tells us the deviation of our derived conductivity from the true value. We consider a typical $s(V)$ contour of the form $s(V)=s_0+a|V|$ with $s_0=5$ Å and $a=1$ Å/V, and we take $V'=0$ V and $V=3$ V. The result of this computation is that the exponential term in Eq. (A16) has a value of 2.5 and the prefactor has a value of 1.8, so that the total deviation of the derived conductivity from the true value is a factor of 4.5. We emphasize, however, that over the same range of 0–3 V, the conductivity at a fixed separation of 8 Å varies by a factor of 33.8, so that the error in our derived conductivity is still a relatively small proportion of the total variation. For tunneling between nonmetallic electrodes, the values of $\partial\kappa/\partial V|_s$ should remain essentially the same (since they are determined mainly by the vacuum barrier), but the values of $I_0(V)$ and $\sigma_0(V)$ in Eq. (A15) will change. The maximum value of $f(V)$ occurs when the second terms in both the numerator and denominator of Eq. (A15) are large compared to the first terms, in which case the above numerical example yields of factor of 2.3 for the prefactor. Thus, we conclude, in general, that the results for the conductivity at constant s will tend to overestimate the total variation of the true conductivity, by as much as an order of magnitude over a measurement range of several volts. Since $\partial\kappa/\partial V|_s$ generally varies smoothly with voltage, then this error will also vary smoothly with voltage and hence will not introduce any significant features in the conductivity spectrum. Thus, so long as one does not interpret the absolute magnitude of the conductivity too literally, then our analysis method provides a rigorous and reliable method for normalizing the conductivity spectra.

---

[*] Permanent address: The University of Texas at Austin, Department of Physics, Austin, TX 78712-1081.

[1] M. D. Kirk, J. Nogami, A. A. Baski, D. B. Mitzi, A. Kapitulnik, T. H. Geballe, and C. F. Quate, Science **242**, 1673 (1988).

[2] C. K. Shih, R. M. Feenstra, J. R. Kirtley, and G. V. Chandrashekhar, Phys. Rev. B **40**, 2682 (1989).

[3] C. Wang, B. Giambattista, C. G. Slough, R. V. Coleman, and M. A. Subramanian, Phys. Rev. B **42**, 8890 (1990).

[4] X. L. Wu, Z. Zhang, Y. Wang, and C. M. Lieber, Science **248**, 1211 (1990).

[5] Y. Gao, P. Lee, P. Coppens, M. A. Subramanian, and A. W. Sleight, Science **241**, 954 (1988).

[6] R. M. Feenstra, J. A. Stroscio, J. Tersoff, and A. P. Fein, Phys. Rev. Lett. **58**, 1192 (1987).

[7] R. M. Feenstra and J. A. Stroscio, Phys. Scr. T **19**, 55 (1987).

[8] M. Tanaka, T. Takahashi, H. Katayama-Yoshida, S. Yamazaki, M. Fujinami, Y.Okabe, W. Mizutani, M. Ono, and K. Kajimura, Nature **339**, 691 (1989).

[9] T. Hasegawa and K. Kitazawa, Jpn. J. Appl. Phys. **29**, L434 (1990).

[10] S. Massidda, J. Yu, A. J. Freeman, H. Krakauer, and W. E. Pickett, Phys. Rev. Lett. **60**, 1665 (1988).

[11] C. G. Olson, R. Liu, A. B. Yang, D. W. Lynch, A. J. Arko, R. S. List, B. W. Veal, Y. C. Chang, P. Z. Jiang, and A. P. Paulikas, Science **245**, 731 (1989).

[12] B. O. Wells *et al.*, Phys. Rev. Lett. **65**, 3056 (1990); B. O. Wells (private communication).

[13] C. K. Shih, E. Kaxiras, R. M. Feenstra, and K. C. Pandey, Phys. Rev. B **40**, 10044 (1989); R. M. Feenstra and P. Mårtensson, Phys. Rev. Lett. **61**, 447 (1988).

[14] C. K. Shih, R. M. Feenstra, and P. Mårtensson, J. Vac. Sci. Technol. A **8**, 3379 (1990).

[15] R. S. Becker, J. A. Golovchenko, and B. S. Swartzentruber, Phys. Rev. Lett. **55**, 987 (1985); J. A. Stroscio, R. M. Feenstra, and A. P. Fein, *ibid.* **57**, 2579 (1987).

[16] For example, I. P. Batra and S. Ciraci, J. Vac. Sci. Technol. A **6**, 313 (1988).

[17] G. Binnig, H. Rohrer, Ch. Gerber, and E. Weibel, Phys. Rev. Lett. **49**, 57 (1982).

[18] G. Binnig, N. Garcia, H. Rohrer, J. M. Soler, and F. Flores, Phys. Rev. B **30**, 4816 (1984).

[19] R. M. Feenstra, J. A. Stroscio, and A. P. Fein, Surf. Sci. **181**, 295 (1987).

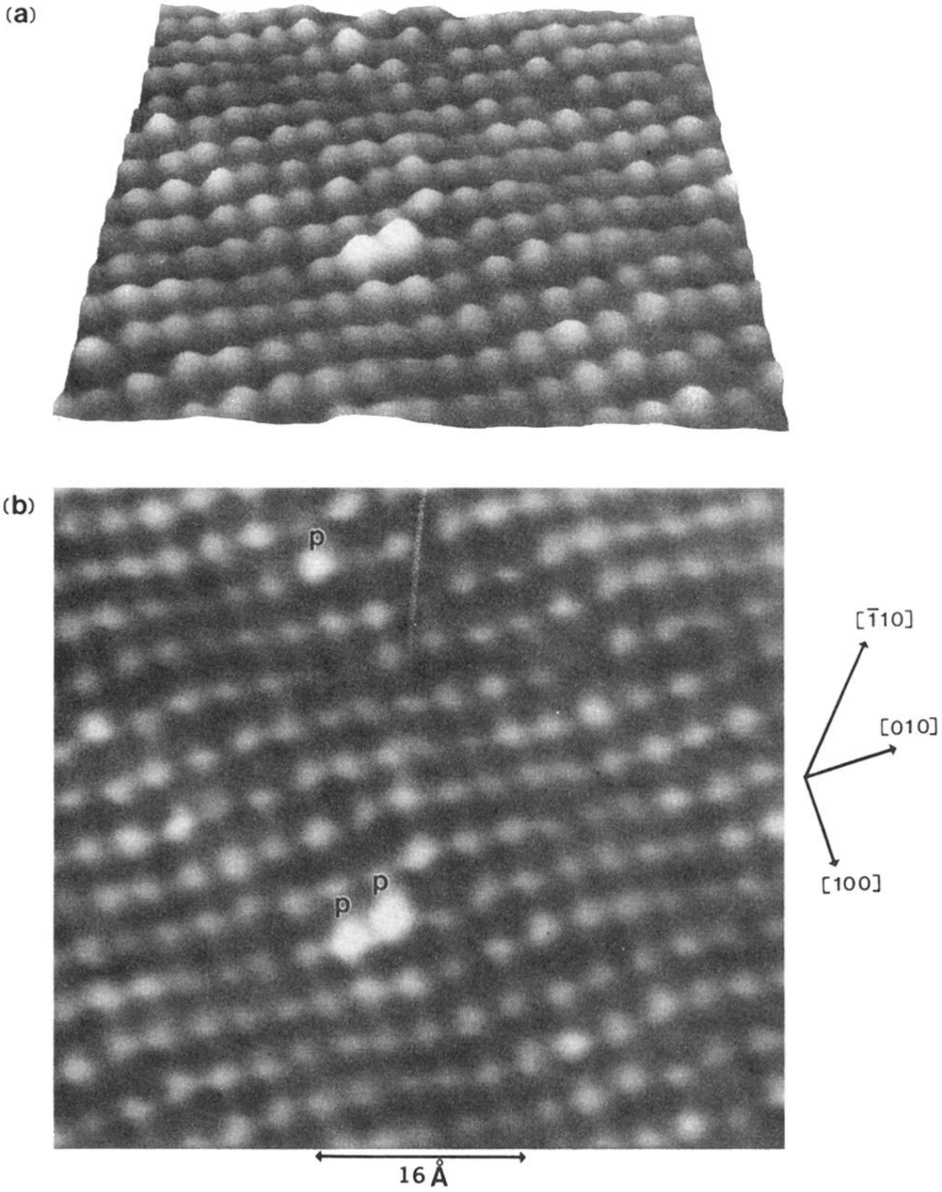

FIG. 1. (a) Perspective view and (b) top view of a STM image taken at a sample bias of -0.75 V. The pervoskite axes are labeled as [100] and [010], and the incommensurate superstructure direction **b** is labeled as [$\bar{1}$10]. The protrusions are labeled as *P*.

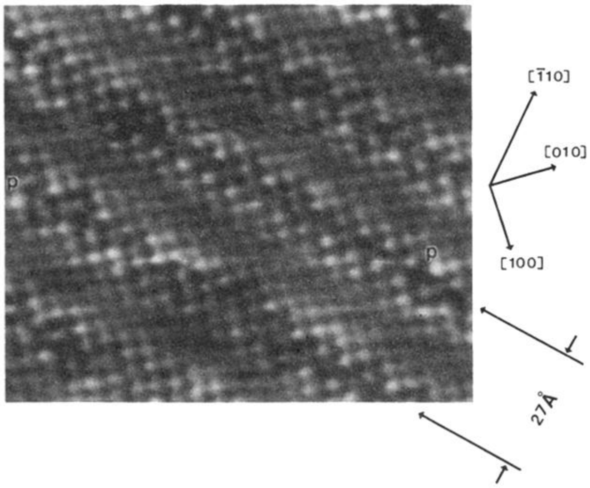

FIG. 2. Top view of a STM image taken at a sample bias of -1.25 V. The depressed atomic rows are marked by the long arrows. Single-atom protrusions are labeled as *P*.

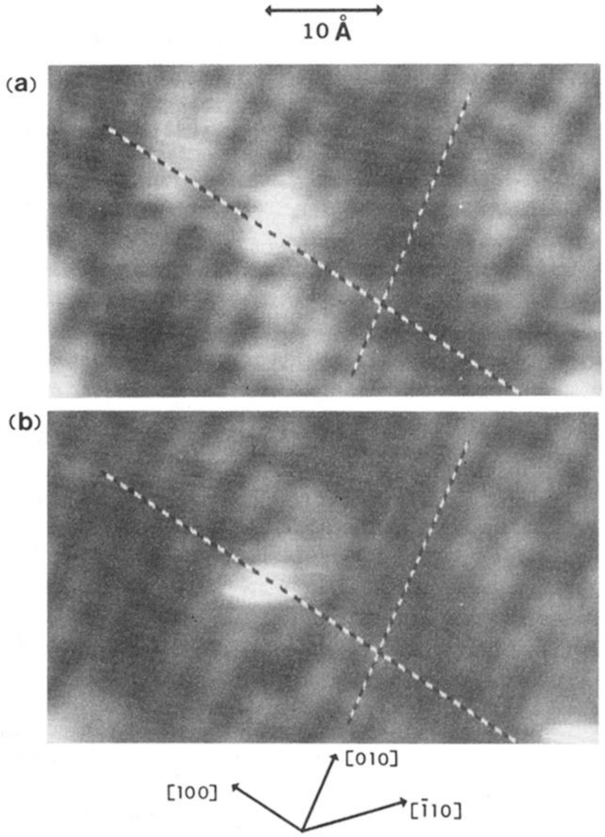

FIG. 3. STM images recorded simultaneously at (a) −1.75 and (b) 1.75 V. The crosshairs are located in identical locations in both images.